HHS Public Access

Author manuscript

Phys Med Biol. Author manuscript; available in PMC 2022 February 11.

Published in final edited form as:

Phys Med Biol. ; 66(4): 045025. doi:10.1088/1361-6560/abd592.

A layered single-side readout DOI TOF-PET detector

L Bläckberg[1], **S Sajedi**[1], **G El Fakhri**[1], **H Sabet**[1]

[1]Gordon Center for Medical Imaging, Department of Radiology, Massachusetts General Hospital & Harvard Medical School, Boston, MA, USA

Abstract

We are exploring a scintillator-based PET detector with potential of high sensitivity, DOI capability, and timing resolution, with single-side readout. Our design combines two previous concepts: 1) Multiple scintillator arrays stacked with relative offset, yielding inherent DOI information, but good timing performance has not been demonstrated with conventional light sharing readout. 2) Single crystal array with one-to-one coupling to the photodetector, showing superior timing performance compared to its light sharing counterparts, but lacks DOI. The combination, where the first layer of a staggered design is coupled one-to-one to a photodetector array, may provide both DOI and timing resolution and this concept is here evaluated through light transport simulations. Results show that: 1) Unpolished crystal pixels in the staggered configuration yield better performance across all metrics compared to polished pixels, regardless of readout scheme. 2) One-to-one readout of the first layer allows for accurate DOI extraction using a single threshold. The number of MPPC pixels with signal amplitudes exceeding the threshold corresponds to the interaction layer. This approach was not possible with conventional light sharing readout. 3) With a threshold of 2 optical photons, the layered approach with one-to-one coupled first layer improves timing close to the MPPC compared to the conventional one-to-one coupling non-DOI detector, due to effectively reduced crystal thickness. Single detector timing resolution values of 91, 127, 151 and 164 ps were observed per layer in the 4-layer design, to be compared to 148 ps for the single array with one-to-one coupling. 4) For the layered design with light sharing, timing improves with increased MPPC pixel size due to higher signal per channel. In conclusion, the combination of straightforward DOI determination, good timing performance, and relatively simple design makes the proposed concept promising for DOI-TOF PET detectors.

1. Introduction

Positron emission tomography (PET) is an imaging modality able to provide functional information related to biological processes in the body which has implications for a number of diseases. For brain imaging in particular, PET can be used to both detect cancer and to aid in diagnosis of neurodegenerative diseases such as dementia [1], Alzheimer's disease [2], and Parkinson's disease [3]. In all these cases early diagnosis is key for good prognosis which emphasizes the value of the availability of high-performance imaging. Furthermore, the significance of the modality is increasing given the continuous development of novel

LBlackberg@MGH.Harvard.edu.

radiopharmaceuticals [4, 5] and analysis methods [6, 7]. There are currently a large number of ongoing hardware developments driven by the limitations of conventional Whole-Body PET (WB-PET) scanners. Examples include high coverage WB-PET systems that are able to image the whole body without the need for patient bed translation, referred to as total body PET [8], as well as organ specific scanners such as brain dedicated PET [9] and breast dedicated PET [10, 11].

Brain dedicated scanners are motivated by the fact that the resolution and sensitivity of conventional WB-PET is not high enough to accurately image small brain structures [9]. Designing a scanner that targets the brain alone allows to reduce the bore size which will lead to less resolution degradation from annihilation photon noncollinearity. The geometric sensitivity for the brain can also be increased without excessive use of detector material. There are a number of scanner geometries being explored including small-bore cylindrical systems [12, 13] as well as systems with unconventional geometries such as helmet- or hat-like PET [14–16], or a wearable PET system [17, 18]. The main purpose of the unconventional geometries is to increase sensitivity compared to purely cylindrical geometries.

For a scanner configuration with small to medium bore size and/or an unconventional geometry, Depth of Interaction (DOI) capability of the detectors in use is more important compared to WB-PET due to the increased probability of oblique angles of incidence on the detector face. The parallax error caused by mapping all events to the center of each detector element is manifested as resolution degradation at the Field of View (FOV) periphery. This blurring increases with crystal thickness, resulting in a tradeoff between sensitivity and spatial resolution unless the interaction depth in the detector can be determined. High resolution across the whole FOV is especially important in brain imaging due to the off-center location of the cerebral cortex. Currently developed brain dedicated systems therefore employ 2–4 levels of DOI achieved through a variety of approaches such as crystal layers with different decay times, varied dopant concentration or varied reflector configurations [9]. In addition to these concepts there are also other approaches for DOI determination including dual-end readout, monolithic crystals with depth dependent light spread [19–26], laser processed crystals [27–35] as well as staggered, or relative offset detectors which is the concept that we are exploring further in this work [36–39].

Another key feature in PET is Time-of-Flight (TOF), which has been shown to improve signal to noise ratio (SNR) in WB-PET by effectively increasing the system sensitivity [40]. The majority of TOF-PET detectors that have been developed are for WB-PET. Smaller bore systems such as brain dedicated PET have higher requirements on the coincidence timing resolution (CTR) needed for effective use of the TOF information to improve image quality. There has been research showing that TOF can be beneficial also for smaller systems, and it might be favorable to use thinner detectors without DOI but with TOF compared to thicker detectors with DOI but without TOF, as the TOF information can compensate for the loss in detection efficiency and DOI degradation is less of an issue for thinner crystals [41]. TOF can also be used to compensate for missing view angles as might be the case in unconventional and asymmetrical geometries and those with limited angular coverage [42–45].

We are aiming to develop a detector with both TOF and DOI capability, as well as high sensitivity and single-side readout to reduce system complexity and cost. This is a challenging task given the many trade-offs that typically must be made between these metrics. Many proposed designs that show good performance have a high level of complexity due to a large number of readout channels for example in dual-end and side-readout configurations [46–48].

The approach behind the detector concept studied in this work is to combine two conventional detector designs. The first is the staggered detector consisting of stacked scintillator arrays relatively offset by half pixel pitch, which has inherent DOI information due to layer dependent scintillator light spread. By employing a center of gravity algorithm to the readout signals, pixel maps from individual detector layers will be shifted from one another making 3D positioning possible in a single-side readout configuration. However, this design has typically been read out using light sharing schemes and has not been demonstrated to provide good timing resolution. To the best of our knowledge, previous investigations of this detector configuration have not been able to provide good CTR, or timing has simply not been considered as the target application has been small animal PET where the sub-10 cm bore size makes the usefulness of TOF information limited given the CTR achievable using todays detector technologies.

The second design is the single scintillator array one-to-one coupled to a photodetector array, which has been shown to provide superior timing performance compared to its light sharing counterparts, but the design lacks DOI information.

By combining these concepts into a detector composed of 2 to 4 stacked scintillator arrays that are each offset from neighboring layers by half pixel pitch in one dimension, with one-to-one readout of the first scintillator array it may be possible to combine desirable characteristics of the two previous designs. Our hypothesis is that such configuration should improve timing performance of the staggered detector compared to the conventional light sharing readout schemes, as the light will be spread over a smaller photodetector area. While a 2-layer version of this detector concept is being explored also by other groups [49, 50], in their work the two layers are offset in two dimensions, which is not optimal for timing as light will be spread over more photodetector pixels compared to when the offset is only in one dimension.

In this work we aim to perform a complete performance evaluation for up to 4 layers, with focus on attainable timing and DOI capabilities relative to the staggered detector with light sharing readout and single layer non-DOI detectors with one-to-one coupling. The goal is to determine important design considerations for DOI and TOF optimization, in terms of number of layers, crystal surface properties and the readout scheme used for the scintillation light. Such study has not been reported previously in the literature as most previous work has not focused on timing characteristics of the staggered detector configuration.

There are several factors of a scintillator detector system that affects the timing resolution, including intrinsic timing properties of the scintillator material (rise and decay time as well as the light yield), light collection efficiency and light transport from the interaction point to

the photodetector, response time, uniformity and noise of the photodetector as well as other downstream electronics [51, 52]. However, given the performance of currently available photodetectors, detector timing resolution is ultimately largely limited by the light generation and light transport within the scintillator crystal [53].

Given that also the DOI characteristics of a scintillator detector are largely dependent on the spread of scintillation light within the detector, light transport simulations are a relevant first step for estimation of performance characteristics of new scintillator detector configurations to obtain important guidance for efficient experimental implementation.

This paper presents a series of light transport simulations conducted to compare the performance characteristics of the proposed staggered detector with one-to-one coupling between the first layer and the photodetector with staggered detectors with light sharing readout schemes, and simple single layer detectors with one-to-one coupling. All detector configurations are compared in terms of a range of important performance metrics, including DOI, transversal pixel separation, timing capability, and light collection efficiency. The outcome of this work can be used for further detector optimization and development for specific imaging system geometries and applications.

2. Materials and methods

All simulations presented in this work have been conducted using the Monte Carlo code DETECT2000 [54], which is developed specifically for light transport in scintillator detectors. It should be noted that only optical photons are transported, and hence the gamma interactions themselves were not simulated in this work.

2.1. Simulated detector geometries

All detector configurations in this study are based on Cerium doped Lutetium Yttrium Oxyorthosilicate (LYSO:Ce) with a total crystal thickness of 20 mm. We are investigating using 2 to 4 scintillator array layers, where each layer is offset from its neighboring layers by half pixel pitch in one dimension and the bottom array is coupled one-to-one to a Multi Pixel Photon Counter (MPPC) array, as illustrated in Figure 1. The difference between this design and the conventional staggered detector, lies in the readout scheme of the first scintillator layer. While traditionally light has been read out by light sharing, mainly by using a light guide, here we explore the potential performance gains by using one-to-one coupling between the first crystal layer and the photodetector array, and no light guide. It should also be noted that, as opposed to other work with one-to-one coupling of the first layer [49, 50], we are employing offset between neighboring layers only in one dimension with the reasoning that timing should be improved when light is shared between fewer MPPC pixels.

In the 2-layer design each crystal layer is 10 mm thick, in the 3-layer design each layer is 6.67 mm thick and in the 4-layer design each layer is 5 mm thick, totaling 20 mm in all cases. For comparison, the same crystal arrangements were simulated also with light sharing between the first crystal layer and the photodetector array. In addition, single layer detectors

were simulated with the same set of readout schemes. All readout schemes implemented for the crystal/MPPC coupling are illustrated in Figure 2.

Given a target intrinsic transversal resolution of 2 mm, our design is based on 2 mm pixel size (2.2 mm pitch) of both the crystal and MPPC array. The reflector thickness was chosen as 0.2 mm to match the MPPC array dead space. For consistency, this reflector thickness was kept for all implemented detector configurations. The light sharing schemes were simulated with different pixel size combinations: 2.2 mm pixels for both crystal and MPPC pixel pitch with readout scheme C (see Figure 2) and a more conventional readout scheme with 4 crystal pixels per MPPC pixel (arrangement B in Figure 2). Although not very common in existing detectors, readout scheme C was evaluated to be able to study the influence of light sharing vs one-to-one coupling between the first crystal layer and the MPPC array, with crystal pitch and MPPC pitch constant. This way, the effect of the light readout scheme can be studied without considering differences in overall detector dimensions. For the more common readout scheme B, both 3.2- and 4.2-mm pixel pitch was used for the MPPC array, corresponding to 1.6- and 2.1-mm pitch for the respective crystal pixels. For all light sharing schemes, a 1 mm thick light guide was used. Per each detector configuration, the quality of the side surfaces of the crystal pixels was varied. Specifics of the implemented detector configurations and the naming convention used throughout the rest of this paper, are summarized in Table 1.

2.2. Simulation parameters

2.2.1 LYSO:Ce crystal array—The LYSO:Ce scintillator material was modelled with a refractive index (RI) of 1.82 at its wavelength of maximum emission (420 nm). Consistent with our previous simulation work of this material, we used an optical absorption length of 40 cm and optical scattering in the crystal bulk was neglected [31, 55]. The entrance and exit surfaces of each pixel were simulated as polished in all cases, and the side surfaces were simulated with two different surface properties: polished and unpolished. The polished surfaces were simulated with the POLISH surface model in DETECT2000, corresponding to 100% specular reflection. The unpolished surfaces were modeled using the UNIFIED surface model implemented in DETECT2000 [56]. Here 100% specular lobe reflection was used with σ_α=20°, where the parameter σ_α corresponds to the standard deviation of a Gaussian distribution of surface normals around the nominal surface normal. Each crystal pixel was simulated with an external diffuse reflector with a reflection coefficient of 0.98, corresponding to 3 layers of Teflon tape [57]. Transport of optical photons within the reflector material was not considered, and optical photons not subject to reflection were treated as absorbed in the reflector material. The scintillator decay was incorporated in the simulations as a sum of one rising and two decreasing exponentials represented by the probability distribution function outlined in Eq. (1), with τ_1= 21.5 ns, τ_2= 43.8 ns, τ_R= 68 ps, α_1= 0.13, and α_2= 0.87 [58].

$$f(t) = \left(\frac{1}{\alpha_1\tau_1 + \alpha_2\tau_2 - \tau_R}\right)\left(\sum_{i=1}^{2} \alpha_i e^{(-t/\tau_i)} - e^{(-t/\tau_R)}\right) \quad (1)$$

Where $\tau_1$and τ_2, are the decay constants of the decreasing exponentials, α_1 and α_2 are their relative weights, and τ_R is the time constant of the rising exponential.

2.2.2 Light guide and optical grease—All interfaces between individual crystal layers, crystal/light guide, and light guide/photodetector surfaces were coupled with optical grease with a thickness of 100 μm and RI=1.47. Where applicable, the light guide was modeled with a thickness of 1 mm and RI=1.52.

2.2.3 MPPC array—MPPC arrays with 3 different active pixel areas (2×2, 3×3 and 4×4 mm^2) were implemented. In all cases the dead space between pixels was 0.2 mm. For the OTO and OTOS designs only the 2x2 mm^2 MPPC pixel size was used but for the light sharing configurations (LS, LSS) all 3 sizes were implemented depending on the readout scheme, as indicated in Table 1. The arrays were simulated with a 100 μm thick entrance window with RI=1.57. Optical photons impinging on the active MPPC area were treated as counted with a 45% quantum efficiency [59]. Photons impinging on the dead space were subject to specular reflection with a 30% probability and absorption with 70% probability. This setting was based on our conversations with the manufacturer.

2.3. Simulation procedure

Gamma interaction events were simulated throughout the detector thickness in representative pixels, as illustrated in Figure 3. In each location 1000 gamma events were randomly distributed across the pixel cross section within a 0.25 mm slab in the Z-direction. Due to the offset between layers, the distributions of transversal X-Y coordinates were shifted accordingly between each layer. The procedure was repeated every 1 mm in the Z-direction. Each gamma event was simulated as a point source of 15000 optical photons emitted isotropically, corresponding to the absorption of 511 keV gamma in LYSO:Ce, with an assumed light yield of ~30k optical photons per MeV as the value typically reported by crystal manufacturers [60, 61]. Note that the light yield of a given LYSO crystal depends on the manufacturer as well as the doping type and concentration, but the used value was chosen as the generally quoted number in the field. Note further that the simulations only entail photo peak events and the effect of Compton scatter is not evaluated in this work.

In addition, a separate set of flood map simulations were performed for the staggered detector configurations (OTOS and LSS) to assess the pixel separation also in the XY dimension. For feasible simulation times the timing properties of each individual optical photon were not recorded in these simulations. Due to symmetry, gamma events (implemented as isotropic point sources of 15000 optical photons) were simulated only in one quarter of the detector. This approach yielded events in 4x4, 4x4, 4x4 and 3x4 crystal pixels for each respective layer to include central pixel rows/columns for layers 2–4 with uneven number of pixels in one or both dimensions. Interaction locations were randomly distributed across the pixel cross sections, with a separation of 1 mm in the Z-direction. In total 16000 events (12000 in layer 4 of the 4-layer designs) were simulated per interaction depth.

2.4. Extracted performance metrics

Per each detector configuration, a range of performance metrics were extracted as described in the following subsections.

2.4.1 Depth of Interaction—DOI capability was assessed as a function of transversal interaction position by studying the light signatures on the photodetector array from individual gamma events. Figure 4 illustrates the expected signal patterns from the 4-layer design with one-to-one readout of the first layer (OTOS-4). This schematic translates also to the 2- and 3-layer designs (OTOS-2,3) if layers are removed from the top. We are proposing a DOI positioning algorithm based on the fact that the signal strength of the 1 (layer 1), 2x1 (layer 2), 2x2 (layer 3) or 3x2 (layer 4) maximum signals should always be significantly larger compared to the signals from the rest of the MPPC array. In these circumstances straightforward DOI classification can be performed by counting the number of MPPC pixels with signal amplitudes exceeding a given threshold, expressed as a percentage of the sum signal from the complete array. In this work we test the algorithm with a threshold based on the distribution of signal amplitudes in each MPPC pixel. The threshold is set at the midpoint between the lower 1 σ bound of the lowest of the 1,2, 4 or 6 primary signal amplitudes across the detector, and the upper 1 abound of the highest signal amplitude of the remaining signals. In the analysis presented in Section 3.1 the DOI level was determined based on the number of signals above the threshold, according to: layer 1=1 signal, layer 2=2 signals, layer 3=3–4 signals, and layer 4=5–6 signals. Note that 3–4 and 5–6 signals were used instead of 4 and 6 for respective layers 3 and 4, as this yielded higher positioning accuracy.

2.4.2 Flood map—For the OTOS design there is one-to-one correspondence between the first crystal layer and the MPPC array, but for events in the outer layers light is shared between multiple MPPC pixels, as described in Figure 4. For these layers the transversal interaction location can be determined based on the center of gravity of the measured MPPC signals.

For the flood source data described in Section 2.3 the interaction locations (x_{ev},y_{ev}) of all events were estimated using a center of gravity algorithm on the MPPC signals, as described in Eq. (2).

$$x_{ev} = \frac{\sum_{i=1}^{M} m_i x_i}{\sum_{i=1}^{M} m_i},\ y_{ev} = \frac{\sum_{j=1}^{N} n_j y_j}{\sum_{i=1}^{N} n_j} \tag{2}$$

where M and N are the number of MPPC elements in each dimension, (x_i, y_j) are the center coordinates of each MPPC pixel, m_i is the total signal amplitude in column i, and n_j is the total signal amplitude in row j. The resulting event coordinates in the detector were histogrammed to obtain flood maps for each of the staggered detectors.

2.4.3 Light collection efficiency—The light collection efficiency (LCE), defined as the fraction of emitted optical photons per event reaching the active area of the photodetector, was calculated as a function of event position for each detector configuration.

Note that in this definition the LCE is independent of the quantum efficiency of the photodetector.

2.4.4 Timing resolution—The timing resolution of a scintillator detector is governed by the rise and decay times of the scintillator material in use, the light yield and the light collection efficiency, response time of the photodetector, and timing properties of the downstream electronics [51, 52]. This paper aims to investigate the effect that detector geometry has on timing performance, and hence the focus of the analysis is on the timing components related to the scintillator material and the detector geometry. Consequently, the simulations only incorporate the time jitter components stemming from scintillator rise and decay time and the light transport from the gamma interaction location to the photodetector. Other contributions such as photodetector response time and dark counts are not included in the simulations, as they should affect all studied geometries in the same way. In the simulations, a delay between gamma interaction and optical photon emission was sampled for each optical photon from the probability distribution function given by Eq. 1. In addition, the transit time between emission and detection at the MPPC array was recorded. The two delay components were summed per optical photon to yield a total time delay between gamma interaction and detection of the optical photon at the photodetector.

For each simulated event, the delays associated with each optical photon were sorted and the delay between the gamma interaction and the time point for the first MPPC pixel to reach a given threshold of n optical photons was extracted. The value of n was varied from 2 to 10 optical photons.

A Gaussian function was fitted to the distribution of delays across given sets of events, and the centroid (i.e., average delay) and FWHM (i.e., time jitter in the delay) were extracted and compared across geometries. Note that this time jitter corresponds to the jitter component from light transport and scintillator decay, which will contribute to the total time jitter in the final signal of a real detector that contains contributions also from the other components of the signal chain. Single detector resolution values were determined in this way per layer in each of the designs. Average timing resolution values per configuration were also calculated by weighting the timing resolution in each layer with the interaction probability of 511 keV gamma rays in the given layer. Given that the photon flux decreases exponentially with distance from the entrance surface of the detector, the weights were calculated based on the individual layer thicknesses and attenuation coefficients at 511 keV extracted from the XCOM database [62]. The weights used were 42.6%, 27.7%, 18.1% and 11.7% for the 4-layer design, 53.2%, 30.0% and 16.8% for the 3-layer design, and 70.2% and 29.8% for the 2-layer design, respectively.

3. Results

In the following sections, the simulated detector configurations are compared across the performance metrics defined in Section 2.4. Focus is given to the OTOS-2,3,4 configurations being the main detector concept studied in this paper. The other readout schemes will be addressed mainly in terms of timing performance given the lack of such information in the current literature.

3.1. DOI

The light signatures predicted in Figure 4 were confirmed by the simulations, as manifested by the light distributions shown in Figure 5. Note that this figure, and the following discussion, corresponds to the staggered design with one-to-one coupling between the first layer and the photodetector (OTOS). It can be seen that from events in layer 1, 1 MPPC pixel measures the majority of the light, from layer 2 the majority of the light is shared equally between 2 MPPC pixels, from layer 3 light is divided between 4 MPPC pixels, and from layer 4 between 6 MPPC pixels. In the latter case, 2 MPPC pixels get a higher signal compared to the other 4. Given that these 1, 2, 4 or 6 dominating signals are always easily separated from those associated with the rest of the MPPC array, the transversal pixel position can be determined from the center of gravity based on these signals, and a transversal resolution corresponding to the pixel size can be achieved (as will be shown in Section 3.2.). Similar signal patterns are observed both in the center, edge, and corner for all studied designs, which bodes well for the DOI classification algorithm proposed in Section 2.4. This algorithm was tested for each OTOS configuration using a single threshold (indicated in each subplot of Figure 5) for the whole detector. The resulting DOI positioning accuracies are summarized in Table 2. As a result of the smaller error bars (i.e., spread in light distribution across events in a given crystal) unpolished pixels yield better DOI positioning accuracy compared to polished pixels. For unpolished pixels, 100% of the events are correctly positioned for OTOS-2 and OTOS-3, regardless of interaction layer. For OTOS-4 there is a slight degradation in positioning accuracy in the fourth layer (for center and edge 1 pixels) and first layer (for edge 2 and corner pixels). For polished pixels in the OTOS-2 configuration the positioning accuracy is >99% throughout the detector. The corresponding number for OTOS-3 is >96%. The two central layers of OTOS-4 also yield high (>95%) positioning accuracy, but significant degradation is observed in the first and fourth layers.

However, if the threshold for central pixels is set purely based on the distribution of MPPC signal amplitudes in the central pixels, the threshold can be lowered to 7.8% of the total signal amplitude (from 10.1%) to achieve positioning accuracy > 99% for all layers in this region. During the analysis, it was observed that the mispositioned events were found mainly close to the layer interfaces, which is expected as the light signatures are more likely to be distorted close to these discontinuities.

Figure 6 shows a selection of the corresponding light signatures for the staggered design with light sharing readout of the first layer (LSS). Only data for unpolished pixels are shown, but similarly as for the OTOS design polished pixels yield similar average light signatures, but with larger spread between events within a given pixel/layer, resulting in larger error bars compared to unpolished pixels. Furthermore, results are shown only for the 2.2/2.2 and the 2.1/4.2 pitch configurations, as the 1.6/3.2 mm pitch yields similar light signatures as 2.1/4.2 given that the same crystal/MPPC pixel ratios are used in both cases. It should be noted however, given that only photo peak events are simulated in this study, the increased inter-crystal Compton scatter rate for the smaller pitch array is not reflected in the obtained data. From Figure 6, it can be inferred that the outlined single relative threshold approach is not possible for either of the LSS designs. For LSS-2 and LSS-3 with 2.1/4.2

mm pixel pitch a single relative threshold could work in the center of the detector, at least for unpolished pixels, but the signal patterns from different layers tend to overlap towards the detector edge. For LSS-4 2.1/4.2 there are problems already for central pixels. For LSS-2,3,4 2.2/2.2 there are no overlaps at the edges, but different decision criteria are needed in different parts of the detector.

3.2. Flood maps

Figure 7 shows flood maps generated for OTOS-4, LSS-4 2.2/2.2 and LSS-4 2.1/4.2. The 4-layers are shown as an example as it offers the highest level of complexity of the studied detectors. The 2- and 3-layer configurations present the same trends as observed for 4 layers. It is seen that one-to-one coupling offers superior pixel separation compared to light sharing readout schemes. In the latter case, the well-known edge effect is apparent, regardless of crystal surface properties. For OTOS-4 all 60 pixels (4x4, 4x4, 4x4 and 3x4 pixels, per layer) are clearly separated. This indicates that 3D positioning could be performed also based on the decoding map, as an alternative to the threshold-based approach proposed in Section 3.1. However, it is apparent that if prior knowledge of the DOI is available through other DOI estimation algorithm such as the threshold-based approach, the decoding map for XY positioning can be split into layer specific maps. These maps would only contain one fourth of the peaks, and the pixel separation would be further increased, which can be important when additional broadening is introduced by scatter and electronic effects. For the light sharing readout scheme, the main issues are at the edge of the detector where, as shown also in Section 3.1, DOI classification is not straightforward using the proposed threshold algorithm, due to overlapping light signatures.

3.3. Light collection efficiency

Table 3 and Table 4 show the average LCE across the total detector depth for central crystal pixels, for all studied detector configurations with one-to-one coupling (Table 3) and light sharing readout schemes (Table 4), respectively. General trends across all designs (OTO/OTOS and LS/LSS) are decreased LCE with increased number of crystal layers and increased LCE for unpolished compared to polished crystal pixels. The LCE was also found to decrease with distance from the MPPC array in all cases. For polished pixels the LCE is more uniform across the crystal depth compared to unpolished pixels. The proposed OTOS design has higher LCE compared to LSS 2.2/2.2 and LSS 1.6/3.2 but marginally lower compared to LSS 2.1/4.2. In general, the readout scheme does however not dramatically affect LCE. Table 5 compares the total LCE averaged over interaction depth between center, edge and corner for the proposed OTOS designs. Regardless of number of layers, the LCE is higher or equal at the edge and corner compared to central pixels, which is manifested also in the timing performance presented in Section 3.4.

3.4. Timing resolution

In Figure 8, the average delay between gamma interaction and the time point when the first MPPC pixel reaches the threshold n, as described in Section 2.4, is shown for 1, 2, 3 and 4 crystal layers as a function of interaction depth. The OTO/OTOS configurations are here compared with the LS/LSS 1.6/3.2 readout scheme.

It can be observed that regardless of readout configuration, the delay increases with distance from the MPPC array, and that the staggered configurations are characterized by an additional jump in the delay for the second, third, and fourth layer compared to single layer designs. It can further be observed that the delay is larger with light sharing readout compared to one-to-one readout, and that unpolished crystal pixels shortens the time delay. It is apparent that a layered design will significantly degrade timing performance if the DOI information is not taken into account as the additional jumps in average delay will effectively increase the total FWHM timing resolution. This can be seen as a 250 ps delay difference between events close to the MPPC (bottom of first layer) and events far from the MPPC (top of fourth layer) for the OTOS-4 design, which can be compared to 150 ps for the OTO configuration (values are given for n=2 and unpolished pixels). However, the fact that DOI can be determined accurately for OTOS allows to treat each layer independently in terms of timing, leading to significantly shortened delay difference between events close to the MPPC and far from the MPPC in a given layer. Hence, there is potential for improvement compared to OTO as the difference in time of arrival between the top and bottom of one layer can decrease with layer thickness.

Figure 9 shows the FWHM time jitter around the average delay for the respective 2-, 3- and 4-layer designs as a function of layer, threshold n, photodetector readout scheme, and surface quality of the crystal pixels. Regardless of design, unpolished pixels yield better performance compared to polished pixels, and the differences between the readout schemes are larger for higher threshold. For LSS 1.6/3.2 and LSS 2.1/4.2 the timing is improved for the increased photodetector size, as this will yield higher signals from individual MPPC pixels, and hence higher probability to reach the threshold earlier. The LSS 2.2/2.2 design consistently performs worse compared to all other designs as light is spread over a larger number of MPPC pixels. In general, OTOS shows higher performance compared to LSS, especially in the layer closest to the MPPC array. However, for the OTOS-4 design there is timing degradation in the outer layers compared to LSS-4 1.6/3.2 and LSS-4 2.1/4.2, which is especially pronounced for high thresholds and unpolished pixels.

Figure 10 shows the variation in timing performance in the center, edge and corner of the detector module for the OTOS-2,3 and 4 designs, respectively. It can be seen that in general timing improves close to the edge, consistent with the LCE trends seen in Table 5, especially close to the MPPC array. The differences across the arrays are also found smaller for unpolished pixels and higher thresholds. Finally, Figure 11 compares the timing performance across all one-to-one coupled designs (OTO and OTOS-2,3,4). It can be seen that for OTOS unpolished pixels are always better performing compared to polished pixels. For the OTO design the opposite trend is seen.

Furthermore, increasing the number of layers improves performance in the layer closest to the MPPC array, as the layer thickness is reduced. For a low threshold of n=2 the performance of the OTOS-3 design can outperform the OTO design throughout the whole detector thickness. For OTOS-4 with the same threshold the performance is only degraded compared to OTO in the outer layer.

Average timing resolution values were calculated as described in Section 2.4, assuming that the detector is placed with the top crystal layer closest to the gamma source. The results presented in Table 6 show that the OTOS-2,3,4 detectors are in favor over the OTO configuration if the pixel surfaces are unpolished and the threshold n is low (i.e., n=2 or 3). For higher thresholds (i.e., n=5 or 10) the only staggered detector configuration with better overall timing performance compared to OTO is OTOS-2.

4. Discussion

This paper investigates performance characteristics of a layered detector design composed of 2+ LYSO:Ce scintillator arrays, each offset from neighboring layers by half pixel pitch in one dimension. This concept has been previously explored mainly with light sharing between the first crystal layer and the photodetector. Here we investigate the possibility of improving performance by instead employing one-to-one coupling between the first crystal layer and the photodetector, with a focus on optimizing timing and DOI performance. The rationale behind this approach is that in conventional single layer detectors one-to-one coupling traditionally outperforms light sharing readout in terms of timing [63].

Furthermore, although the staggered detector is a well-known concept, the timing capabilities of the design have not been studied extensively. In previous work based on light sharing between the photodetector and the first crystal layer, timing has either not been investigated [36, 38, 39] or the presented numbers have been in the 800–900 ps range [37] which is a factor of 3–4 higher compared to what is currently used in conventional WB-PET systems. Previous studies of the 2-layer configuration with one-to-one readout of the first layer, but with layers offset in 2 dimensions which should be sub-optimal in terms of timing, reported experimental CTR values of around 500 ps [49]. The current paper provides a range of relevant performance metrics, including DOI, transversal pixel separation, timing, and LCE, for up to 4 layers of the staggered detector with one-to-one readout of the first layer (OTOS), compared to conventional staggered detectors with light sharing (LSS) and single layer one-to-one coupled detectors (OTO). The study is performed through light transport simulations motivated by the fact that the performance of any scintillator detector is limited by the generation and transport of optical photons.

One major advantage of the proposed OTOS design compared to the conventional LSS design was found to be the possibility of straightforward DOI determination. The OTOS configurations are all characterized by well-defined layer dependent light distribution patterns (see Figure 4 and Figure 5). We propose a DOI positioning algorithm where the relative MPPC signal amplitudes (with respect to the sum of all signal amplitudes across the array) are compared to a single threshold. The number of MPPC pixels above the threshold for a given event is then used to determine the layer of interaction. Results show 100% DOI positioning accuracy throughout the detector for OTOS-2 and OTOS-3 and >91% accuracy for OTOS-4 with unpolished pixels with this method (see Table 2).

The corresponding DOI positioning approach was not possible for the LSS detectors due to overlapping light signatures mainly at the detector edge (for LSS-2,3,4 2.1/4.2), or a need for different classification criteria depending on transversal pixel location (for LSS-2,3,4

2.2/2.2). Problems with accurate positioning at the detector edge have previously been reported for the conventional 4-layer staggered geometry [39], and it is a well-known problem in any detector readout using light sharing.

Note that in a real detector there will be deviations from the somewhat idealistic case studied here, such as gain variations between MPPC pixels. However, this is something that is present regardless of detector configuration or positioning algorithm, and that can be calibrated and compensated for. The clean light signatures of the OTOS design with maximized signal strength per MPPC pixel (compared to LSS) will make it easier to deal with these potential issues. In addition, the flood maps shown in Figure 7 highlight the advantage of the OTOS design also for conventional map-based DOI estimation. This flexibility in available routes for spatial encoding is one of the strengths of the OTOS design when compared to the LSS design.

Another potential benefit of the OTOS design, not explored in this work, is that the well-defined light signatures may also be used for Compton scatter decomposition. A gamma-ray interacting with more than one crystal pixel and/or layer (such as inter-crystal scatter) should result in a light signature that deviates from the clean photo peak signatures described here. One can explore this difference to determine the pixel/layer of the first interaction. This feature can be especially important as the inter-crystal scatter will increase in any detector with smaller pixel cross section and thinner layers [64, 65].

The OTOS and LSS designs have similar LCE with a slight advantage of OTOS and LSS 2.1/4.2 compared to the other LSS configurations (see Table 3 and Table 4). LCE is always around a factor of 2 higher for unpolished compared to polished pixels due to less trapping and bulk absorption. When comparing the LCE across the different LSS designs (Table 4), the LSS 2.1/4.2 configuration yields the highest LCE due to the larger relative active area of the employed photodetector, compared to the other two designs. For the LSS 1.6/3.2 design there is another component of smaller crystal cross-section which also affects LCE and offsets some of the gain from larger active MPPC area compared to the LSS 2.2/2.2 design.

For the OTOS-2,3 and 4 designs with unpolished pixels the average LCE increases slightly towards the edges and corners of the detector (compared to the center), while LCE was found more constant across the array for polished pixels (see Table 5). This is an effect from the fact that the array gets smaller (fewer pixels) with distance from the MPPC array (see Figure 1). The parts of the crystals that are not coupled to the above array are covered by reflector material, resulting in the observed slight increase in LCE. The same trends were observed also in the timing performance.

In terms of timing, the different configurations were compared using the jitter in the time of arrival of the 2^{nd},3^{rd},5^{th} and 10^{th} optical photon detected by the MPPC pixel first triggering the mentioned threshold level.

The factors reflected in this timing metric are the intrinsic timing properties of the scintillator material, including the rise and decay constants of LYSO:Ce, and the travel time from the interaction location to the photodetector. Other factors such as time variations in the photodetector response, dark counts, non-uniform time response between photodetector

elements, and time jitter in the downstream electronics were not included in the simulations. Hence the values should be interpreted relative to each other rather than as final single detector timing resolution values. Given that the factors mentioned above should affect all studied configurations equally, and that timing resolution is ultimately limited by the time distribution in the arrival times of optical photons at the photodetector, the results reported here are still valid for detector comparison.

The timing study highlights the second major promising characteristic of the OTOS design, which is the possibility of improving timing resolution compared to a single layer (OTO) detector (see Figure 11). While the fluctuations in time of arrival between events close to and far from the MPPC is larger in the OTOS designs compared to the OTO design, the availability of DOI information can be used to compensate for this difference by considering each layer individually for timing purposes [66].

In accordance with previous work, for OTO it is seen that polished crystals provide better timing performance compared to unpolished crystals in pixels with high aspect ratio [53, 67]. For the staggered approach however, the opposite trend is observed, and timing is improved with unpolished crystal pixels. A similar trend change has been seen by others where in the single layer design unpolished pixels are favorable over polished ones when the crystals are thinner (5 mm) while the opposite is true for thicker (20 mm) ones [67].

Furthermore, timing resolution improves in the crystal layer closest to the MPPC as the total number of layers increases, which corresponds to thinner individual layers (20 vs 5 mm for OTO and OTOS-4, respectively). For a low threshold of 2 optical photons, all layers of the OTOS-2 and OTOS-3 designs with unpolished pixels outperform the conventional single layer design (OTO) in terms of timing. For OTOS-4 there is a degradation in the outermost 5 mm layer compared to OTO. With increased detection threshold, the benefit of the OTOS design compared to OTO is lost, except for the layer closest to the photodetector, and when using polished pixels timing is always degraded compared to single layer detectors.

It should also be noted that the DOI information available with the OTOS designs can be used for DOI compensation to further improve the final estimate of the source location along the line of response compared to non-DOI detectors. The reason is that in addition to providing a more accurate timestamp, it also provides a more accurate estimate of the gamma interaction location within the detector [51].

Average timing resolution values were calculated per design configuration, further highlighting the advantage of the OTOS design compared to the OTO design for low thresholds and unpolished pixels (see Table 6). Noteworthy is that one could think of applications where the whole detector can be flipped to have the MPPC closer to the FOV in order to take advantage of better timing performance.

In this work optical scatter in the crystal bulk was neglected. This was done largely due to difficulties in finding accurate values for the scatter length [68], in combination with the relatively small size of the studied detectors which should limit the effect of bulk scatter. Additional simulations were performed for the OTO and OTOS-4 designs with varying scatter length in order to estimate the effect of this assumption on the presented results. The

effect of bulk scattering was found negligible except when going down to a scatter length of 100 mm, which should be considered an extreme case. However even here the trends between the different detector configurations remained the same.

Other studies have shown that thinner layers close to the entrance side of the detector may be beneficial to minimize the parallax error with layered detectors [69–71]. Preliminary simulations of the OTOS-2 detector with 12+8 mm layers showed some degradation in timing resolution in the first layer (8.9% for unpolished pixels and 0.5% for polished pixels with n=2) due to increased layer thickness, but slight improvements in the second layer (1.6–1.7 % for n=2), when compared to the 10+10 mm layers explored in this work. It should be noted that the optimal layer thickness combination is strongly dependent on the geometry of the given scanner. Hence, any further optimization with respect to variations in individual layer thicknesses needs to be done with a particular scanner geometry and application in mind.

Ultimately, the final application for the detectors should be driving which metrics are most important for the system as a whole, and the interplay between DOI, timing, sensitivity, and intrinsic transversal resolution should guide which detector is most suitable for a given imaging system.

5. Conclusions

This work showcases a range of important performance metrics for the staggered detector with one-to-one readout of the first scintillator layer, compared to other conventional detector configurations.

The design is characterized by well-defined layer dependent light signatures with light confined to few MPPC pixels, which can have benefits for timing, event positioning, and potentially inter-crystal Compton scatter decomposition. We show that the proposed design has the potential to improve timing compared to the gold standard single layer detector with one-to-one coupling, and that it can provide flexible and straightforward DOI determination compared to its light sharing counterparts.

When comparing this design to other detector approaches able to provide both DOI and timing information, the practicality and relative simplicity of the concept presented here should be emphasized, as this ultimately will drive the cost of any system level implementation.

We believe that the proposed design can be interesting both for brain PET as well as other applications requiring high spatial resolution, high sensitivity, and TOF information, such as WB-PET, breast dedicated PET, and other organ- specific PET systems with limited angle detector coverage.

Acknowledgements

This work was supported in part by NIH grant R21EB023391. The authors would like to thank Abhishikth Devabhaktuni for help with the data analysis.

References

[1]. Sarikaya I, Sarikaya A, and Elgazzar AH, "Current Status of (18)F-FDG PET Brain Imaging in Patients with Dementia," J Nucl Med Technol, vol. 46, no. 4, pp. 362–367, 12 2018, doi: 10.2967/jnmt.118.210237. [PubMed: 30076253]

[2]. Marcus C, Mena E, and Subramaniam RM, "Brain PET in the diagnosis of Alzheimer's disease," Clin Nucl Med, vol. 39, no. 10, pp. e413–22; quiz e423–6, 10 2014, doi: 10.1097/RLU.0000000000000547. [PubMed: 25199063]

[3]. Pavese N, "PET studies in Parkinson's disease motor and cognitive dysfunction," Parkinsonism Relat Disord, vol. 18 Suppl 1, pp. S96–9, 1 2012, doi: 10.1016/S1353-8020(11)70031-1. [PubMed: 22166468]

[4]. Acuff SN, Mathotaarachchi S, Zukotynski K, Osborne D, Subramaniam R, and Alzheimer's Disease Neuroimaging I, "Clinical and Technical Considerations for Brain PET Imaging for Dementia," J Nucl Med Technol, vol. 48, no. 1, pp. 5–8, 3 2020, doi: 10.2967/jnmt.118.220087. [PubMed: 31182663]

[5]. Ibrahim N et al., "The sensitivity and specificity of F-DOPA PET in a movement disorder clinic," Am J Nucl Med Mol Imaging, vol. 6, no. 1, pp. 102–9, 2016. [Online]. Available: https://www.ncbi.nlm.nih.gov/pubmed/27069770. [PubMed: 27069770]

[6]. Sepulcre J et al., "Neurogenetic contributions to amyloid beta and tau spreading in the human cortex," Nat Med, vol. 24, no. 12, pp. 1910–1918, 12 2018, doi: 10.1038/s41591-018-0206-4. [PubMed: 30374196]

[7]. Gallivanone F, Della Rosa PA, and Castiglioni I, "Statistical Voxel-Based Methods and [18F]FDG PET Brain Imaging: Frontiers for the Diagnosis of AD," Curr Alzheimer Res, vol. 13, no. 6, pp. 682–94, 2016, doi: 10.2174/1567205013666151116142039. [PubMed: 26567733]

[8]. Cherry SR, Jones T, Karp JS, Qi J, Moses WW, and Badawi RD, "Total-Body PET: Maximizing Sensitivity to Create New Opportunities for Clinical Research and Patient Care," J Nucl Med, vol. 59, no. 1, pp. 3–12, 1 2018, doi: 10.2967/jnumed.116.184028. [PubMed: 28935835]

[9]. Catana C, "Development of Dedicated Brain PET Imaging Devices: Recent Advances and Future Perspectives," J Nucl Med, vol. 60, no. 8, pp. 1044–1052, 8 2019, doi: 10.2967/jnumed.118.217901. [PubMed: 31028166]

[10]. Narayanan D and Berg WA, "Dedicated Breast Gamma Camera Imaging and Breast PET: Current Status and Future Directions," PET Clinics, vol. 13, no. 3, pp. 363–381, 2018/07/01/ 2018, doi: 10.1016/j.cpet.2018.02.008. [PubMed: 30100076]

[11]. Hsu DF, Freese DL, and Levin CS, "Breast-Dedicated Radionuclide Imaging Systems," J Nucl Med, vol. 57 Suppl 1, pp. 40S–5S, 2 2016, doi: 10.2967/jnumed.115.157883. [PubMed: 26834101]

[12]. Yamaya T, Yoshida E, Obi T, Ito H, Yoshikawa K, and Murayama H, "First Human Brain Imaging by the jPET-D4 Prototype With a Pre-Computed System Matrix," IEEE Transactions on Nuclear Science, vol. 55, no. 5, pp. 2482–2492, 2008, doi: 10.1109/TNS.2008.2003252.

[13]. Wienhard K et al., "The ECAT HRRT: performance and first clinical application of the new high resolution research tomograph," IEEE Transactions on Nuclear Science, vol. 49, no. 1, pp. 104–110, 2002, doi: 10.1109/TNS.2002.998689.

[14]. Tashima H and Yamaya T, "Proposed helmet PET geometries with add-on detectors for high sensitivity brain imaging," Phys Med Biol, vol. 61, no. 19, pp. 7205–7220, 10 7 2016, doi: 10.1088/0031-9155/61/19/7205. [PubMed: 27649355]

[15]. Tashima H et al., "Development of the helmet-chin PET prototype," in 2015 IEEE Nuclear Science Symposium and Medical Imaging Conference (NSS/MIC), 31 Oct.-7 Nov. 2015 2015, pp. 1–3, doi: 10.1109/NSSMIC.2015.7582022.

[16]. Sheikhzadeh P, Sabet H, Ghadiri H, Geramifar P, Ghafarian P, and Ay MR, "Concept design and Monte Carlo performance evaluation of HeadphonePET: a novel brain-dedicated PET system based on partial cylindrical detectors," Journal of Instrumentation, vol. 13, p. P07008, 2018.

[17]. Bauer CE et al., "Concept of an upright wearable positron emission tomography imager in humans," Brain Behav, vol. 6, no. 9, p. e00530, 9 2016, doi: 10.1002/brb3.530. [PubMed: 27688946]

[18]. Melroy S et al., “Development and Design of Next-Generation Head-Mounted Ambulatory Microdose Positron-Emission Tomography (AM-PET) System,” Sensors (Basel), vol. 17, no. 5, 5 19 2017, doi: 10.3390/s17051164.

[19]. Ling T, Lewellen TK, and Miyaoka RS, “Depth of interaction decoding of a continuous crystal detector module,” Physics in Medicine and Biology, vol. 52, pp. 2213–2228, 2007. [PubMed: 17404465]

[20]. Lamprou E, Gonzalez AJ, Sanchez F, and Benlloch JM, “Exploring TOF capabilities of PET detector blocks based on large monolithic crystals and analog SiPMs,” Phys Med, vol. 70, pp. 10–18, 2 2020, doi: 10.1016/j.ejmp.2019.12.004. [PubMed: 31935602]

[21]. Marcinkowski R, Mollet P, Van Holen R, and Vandenberghe S, “Sub-millimetre DOI detector based on monolithic LYSO and digital SiPM for a dedicated small-animal PET system,” Physics in Medicine and Biology, vol. 61, no. 5, pp. 2196–2212, 2016/02/23 2016, doi: 10.1088/0031-9155/61/5/2196. [PubMed: 26907952]

[22]. Borghi G, Tabacchini V, Bakker R, and Schaart DR, “Sub-3 mm, near-200 ps TOF/DOI-PET imaging with monolithic scintillator detectors in a 70 cm diameter tomographic setup,” Physics in Medicine & Biology, vol. 63, no. 15, p. 155006, 2018/07/27 2018, doi: 10.1088/1361-6560/aad2a6. [PubMed: 29995639]

[23]. Li Z, Wedrowski M, Bruyndonckx P, and Vandersteen G, “Nonlinear least-squares modeling of 3D interaction position in a monolithic scintillator block,” Phys Med Biol, vol. 55, no. 21, pp. 6515–32, 11 7 2010, doi: 10.1088/0031-9155/55/21/012. [PubMed: 20959686]

[24]. Rato Mendes P et al., “Characterization and performance of monolithic detector blocks with a dedicated ASIC front-end readout for PET imaging of the human brain,” Nuclear Instruments and Methods in Physics Research Section A: Accelerators, Spectrometers, Detectors and Associated Equipment, vol. 633, pp. S33–S35, 2011/05/01/ 2011, doi: 10.1016/j.nima.2010.06.113.

[25]. Etxebeste A, Barrio J, Munoz E, Oliver JF, Solaz C, and Llosa G, “3D position determination in monolithic crystals coupled to SiPMs for PET,” Phys Med Biol, vol. 61, no. 10, pp. 3914–34, 5 21 2016, doi: 10.1088/0031-9155/61/10/3914. [PubMed: 27119737]

[26]. González-Montoro A et al., “Detector block performance based on a monolithic LYSO crystal using a novel signal multiplexing method,” Nuclear Instruments and Methods in Physics Research Section A: Accelerators, Spectrometers, Detectors and Associated Equipment, vol. 912, pp. 372–377, 2018/12/21/ 2018, doi: 10.1016/j.nima.2017.10.098.

[27]. Moriya T et al., “Development of PET detectors using monolithic scintillation crystals processed with sub-surface laser engraving technique,” IEEE Transactions on Nuclear Science, vol. 57, pp. 2455–2459, 2010, doi: 10.1109/TNS.2010.2056387.

[28]. Uchida H, Sakai T, Yamauchi H, Hakamata K, Shimizu K, and Yamashita T, “A novel single-ended readout depth-of-interaction PET detector fabricated using sub-surface laser engraving.,” Physics in medicine and biology, vol. 61, pp. 6635–6650, 2016, doi: 10.1088/0031-9155/61/18/6635. [PubMed: 27541440]

[29]. Panetta JV, Surti S, Singh B, and Karp JS, “Characterization of Monolithic Scintillation Detectors Etched with Laser Induced Optical Barriers,” IEEE Transactions on Radiation and Plasma Medical Sciences, 2018, doi: 10.1109/TRPMS.2018.2875156.

[30]. Hunter WCJ, Miyaoka RS, MacDonald L, McDougald W, and Lewellen TK, “Light-sharing interface for dMiCE detectors using sub-surface laser engraving,” IEEE Transactions on Nuclear Science, vol. 62, pp. 27–35, 2015, doi: 10.1109/TNS.2014.2374075. [PubMed: 25914421]

[31]. Bläckberg L, El-Fakhri G, and Sabet H, “Simulation study of light transport in laser-processed LYSO:Ce detectors with single-side readout,” Physics in Medicine and Biolobgy, vol. 62, no. 21, pp. 0–12, 2017, doi: 10.1088/1361-6528/aa8b39.

[32]. Bläckberg L, Moebius M, El Fakhri G, Mazur E, and Sabet H, “Light Spread Manipulation in Scintillators Using Laser Induced Optical Barriers,” IEEE Transactions on Nuclear Science, vol. 65, no. 8, pp. 2208–2215, 2018, doi: 10.1109/TNS.2018.2809570. [PubMed: 30905974]

[33]. Sabet H and El-Fakhri G, “Novel cost-effective and high-performance modular detectors for emission tomography systems,” 2014 IEEE Nuclear Science Symposium and Medical Imaging Conference Record (NSS/MIC 2014), 2014, doi: 10.1109/NSSMIC.2012.6551932.

[34]. Sabet H, Blackberg L, Ozsahin DU, Sitek A, and El-Fakhri G. A sub-mm spatial resolution LYSO:Ce detector for small animal PET.

[35]. Sabet H, Kudrolli H, Singh B, and Nagarkar VV, "Fabricating high-resolution and high-sensitivity scintillator arrays using Laser Induced Optical Barriers," in 2012 IEEE Nuclear Science Symposium and Medical Imaging Conference Record (NSS/MIC), 27 Oct.-3 Nov. 2012 2012, pp. 4080–4084, doi: 10.1109/NSSMIC.2012.6551932.

[36]. González AJ et al., "The MINDView brain PET detector, feasibility study based on SiPM arrays," Nuclear Instruments and Methods in Physics Research Section A: Accelerators, Spectrometers, Detectors and Associated Equipment, Vol. 818, pp. 82–90, 2016/05/11/ 2016, doi: 10.1016/j.nima.2016.02.046.

[37]. Liu H, Omura T, Watanabe M, and Yamashita T, "Development of a depth of interaction detector for γ- rays," Nuclear Instruments and Methods in Physics Research Section A: Accelerators, Spectrometers, Detectors and Associated Equipment, vol. 459, no. 1, pp. 182–190, 2001/02/21/ 2001, doi: 10.1016/S0168-9002(00)00939-6.

[38]. Chung YH et al., "Monte Carlo simulation of a four-layer DOI detector with relative offset in animal PET," Nuclear Instruments and Methods in Physics Research Section A: Accelerators, Spectrometers, Detectors and Associated Equipment, vol. 626-627, pp. 43–50, 2011/01/11/ 2011, doi: 10.1016/j.nima.2010.10.092.

[39]. Mikiko I et al., "Four-layer DOI detector with a relative offset in animal PET system," in 2007 IEEE Nuclear Science Symposium Conference Record, 26 Oct.-3 Nov. 2007 2007, vol. 6, pp. 4296–4299, doi: 10.1109/NSSMIC.2007.4437066.

[40]. Kadrmas DJ, Oktay MB, Casey ME, and Hamill JJ, "Effect of Scan Time on Oncologic Lesion Detection in Whole-Body PET," IEEE Trans Nucl Sci, vol. 59, no. 5, pp. 1940–1947, 10 2012, doi: 10.1109/TNS.2012.2197414. [PubMed: 23293380]

[41]. Takyu S et al., "Design study of a brain-dedicated time-of-flight PET system with a hemispherical detector arrangement," Phys Med Biol, vol. 65, no. 3, p. 035012, 2 4 2020, doi: 10.1088/1361-6560/ab63ee. [PubMed: 31855854]

[42]. Lee E, Werner ME, Karp JS, and Surti S, "Design Optimization of a TOF, Breast PET Scanner," IEEE Trans Nucl Sci, vol. 60, no. 3, pp. 1645–1652, 6 2013, doi: 10.1109/TNS.2013.2257849. [PubMed: 24078744]

[43]. Sajedi S, Bläckberg L, El Fakhri G, Choi HS, and Sabet H, "Intraoperative radio-guided imaging system for surgical applications," Journal of Nuclear Medicine, vol. 60, no. supplement 1, pp. 317–317, 2019.

[44]. Sajedi S et al., "Limited-Angle TOF-PET for Intraoperative Surgical Application," in 2019 IEEE Nuclear Science Symposium and Medical Imaging Conference (NSS/MIC), 26 Oct.-2 Nov. 2019 2019, pp. 1–4, doi: 10.1109/NSS/MIC42101.2019.9059690.

[45]. Surti S and Karp JS, "Design considerations for a limited angle, dedicated breast, TOF PET scanner," Physics in Medicine and Biology, vol. 53, no. 11, pp. 2911–2921, 2008/05/06 2008, doi: 10.1088/0031-9155/53/11/010. [PubMed: 18460745]

[46]. Yeom JY, Vinke R, and Levin CS, "Side readout of long scintillation crystal elements with digital SiPM for TOF-DOI PET," Med Phys, vol. 41, no. 12, p. 122501, 12 2014, doi: 10.1118/1.4901524. [PubMed: 25471979]

[47]. Han YB, Kang HG, Song SH, Ko GB, Lee JS, and Hong SJ, "SiPM-based dual-ended-readout DOI-TOF PET module based on mean-time method," Journal of Instrumentation, vol. 14, no. 02, pp. P02023–P02023, 2019/02/19 2019, doi: 10.1088/1748-0221/14/02/p02023.

[48]. Cates JW and Levin CS, "Evaluation of a clinical TOF-PET detector design that achieves <100 ps coincidence time resolution," Physics in Medicine & Biology, vol. 63, no. 11, p. 115011, 2018/06/07 2018, doi: 10.1088/1361-6560/aac504. [PubMed: 29762136]

[49]. Belcari N et al., "Design and Detector Performance of the PET Component of the TRIMAGE PET/MR/EEG Scanner," IEEE Transactions on Radiation and Plasma Medical Sciences, vol. 3, no. 3, pp. 292–301, 2019, doi: 10.1109/TRPMS.2019.2906407.

[50]. Camarlinghi N et al., "Evaluation of Algorithms for Photon Depth of Interaction Estimation for the TRIMAGE PET Component," IEEE Transactions on Nuclear Science, vol. 63, no. 1, pp. 70–74, 2016, doi: 10.1109/TNS.2015.2512986.

[51]. Lecoq P, “Pushing the Limits in Time-of-Flight PET Imaging,” IEEE Transactions on Radiation and Plasma Medical Sciences, vol. 1, no. 6, pp. 473–485, 2017, doi: 10.1109/TRPMS.2017.2756674.

[52]. Derenzo SE, Choong WS, and Moses WW, “Fundamental limits of scintillation detector timing precision,” Phys Med Biol, vol. 59, no. 13, pp. 3261–86, 7 7 2014, doi: 10.1088/0031-9155/59/13/3261. [PubMed: 24874216]

[53]. Berg E, Roncali E, and Cherry SR, “Optimizing light transport in scintillation crystals for time-of-flight PET: an experimental and optical Monte Carlo simulation study,” Biomedical optics express, vol. 6, pp. 2220–2230, 2015, doi: 10.1364/BOE.6.002220. [PubMed: 26114040]

[54]. Cayouette F, Laurendeau D, and Moisan C, “DETECT2000: an improved Monte-Carlo simulator for the computer aided design of photon sensing devices,” Proc. SPIE, vol. 4833, pp. 69–76, 2003, doi: 10.1117/12.474315.

[55]. Bläckberg L et al., “Exploring light confinement in laser-processed LYSO:Ce for photon counting CT application,” Phys Med Biol, vol. 64, no. 9, p. 095020, 4 29 2019, doi: 10.1088/1361-6560/ab1213. [PubMed: 30897557]

[56]. Levin A and Moisan C, “A more physical approach to model the surface treatment of \nscintillation counters and its implementation into DETECT,” 1996 IEEE Nuclear Science Symposium. Conference Record, vol. 2, 1996, doi: 10.1109/NSSMIC.1996.591410.

[57]. Janecek M and Moses WW, “Optical reflectance measurements for commonly used reflectors,” IEEE Transactions on Nuclear Science, vol. 55, pp. 2432–2437, 2008, doi: 10.1109/TNS.2008.2001408.

[58]. Gundacker S, Turtos RM, Auffray E, and Lecoq P, “Precise rise and decay time measurements of inorganic scintillators by means of X-ray and 511 keV excitation,” Nuclear Instruments and Methods in Physics Research Section A: Accelerators, Spectrometers, Detectors and Associated Equipment, vol. 891, pp. 42–52, 2018/05/21/ 2018, doi: 10.1016/j.nima.2018.02.074.

[59]. Hamamatsu Photonics KK, “MPPC (Multi-Pixel Photon Counter) S14160/S14161 Series,” 2020.

[60]. Saint-Gobain Crystals. https://www.crystals.saint-gobain.com/sites/imdf.crystals.com/files/documents/lyso-material-data-sheet.pdf (accessed 09/24/20, 2020).

[61]. Epic crystals. http://www.epic-crystal.com/oxide-scintillators/lyso-ce-scintillator.html#:~:text=LYSO%3A%20Ce%20crystal%20crystal%20has,results%20of%2030x30x100%20mm%20crystal. (accessed 09/24/20, 2020).

[62]. Berger MJ et al. XCOM: Photon Cross Section Database (version 1.5) [Online] Available: http://physics.nist.gov/xcom

[63]. Surti S and Karp JS, “Advances in time-of-flight PET,” Phys Med, vol. 32, no. 1, pp. 12–22, 1 2016, doi: 10.1016/j.ejmp.2015.12.007. [PubMed: 26778577]

[64]. Gu Z, Prout DL, Silverman RW, Herman H, Dooraghi A, and Chatziioannou AF, “A DOI Detector With Crystal Scatter Identification Capability for High Sensitivity and High Spatial Resolution PET Imaging,” IEEE Trans Nucl Sci, vol. 62, no. 3, pp. 740–747, 6 2015, doi: 10.1109/TNS.2015.2408333. [PubMed: 26478600]

[65]. Sheikhzadeh P et al., “Development and validation of an accurate GATE model for NeuroPET scanner,” Phys Med, vol. 40, pp. 59–65, 8 2017, doi: 10.1016/j.ejmp.2017.07.008. [PubMed: 28716541]

[66]. Vandenberghe S, Mikhaylova E, D’Hoe E, Mollet P, and Karp JS, “Recent developments in time-of-flight PET,” EJNMMI Phys, vol. 3, no. 1, p. 3, 12 2016, doi: 10.1186/s40658-016-0138-3. [PubMed: 26879863]

[67]. Spanoudaki VC and Levin CS, “Investigating the temporal resolution limits of scintillation detection from pixellated elements: comparison between experiment and simulation,” Physics in Medicine and Biology, vol. 56, no. 3, pp. 735–756, 2011/01/14 2011, doi: 10.1088/0031-9155/56/3/013. [PubMed: 21239845]

[68]. Steinbach CO, Ujhelyi F, and Lörincz E, “Measuring the Optical Scattering Length of Scintillator Crystals,” IEEE Transactions on Nuclear Science, vol. 61, no. 5, pp. 2456–2463, 2014, doi: 10.1109/TNS.2014.2346027.

[69]. Stortz G et al., “Simulation guided optimization of Dual Layer Offset detector design for use in small animal PET,” in 2011 IEEE Nuclear Science Symposium Conference Record, 23–29 Oct. 2011 2011, pp. 3378–3381, doi: 10.1109/NSSMIC.2011.6152612.

[70]. Yong Hyun C, Yong C, Gyuseong C, Yearn Seong C, Kyung-Han L, and Byung-Tae K, “Optimization of dual layer phoswich detector consisting of LSO and LuYAP for small animal PET,” in 2003 IEEE Nuclear Science Symposium. Conference Record (IEEE Cat. No.03CH37515), 19–25 Oct. 2003 2003, vol. 4, pp. 2257–2261 Vol.4, doi: 10.1109/NSSMIC.2003.1352348.

[71]. Teimoorisichani M and Goertzen AL, “Geometry Optimization of a Dual-Layer Offset Detector for Use in Simultaneous PET/MR Neuroimaging,” IEEE Transactions on Radiation and Plasma Medical Sciences, vol. 3, no. 3, pp. 275–284, 2019, doi: 10.1109/TRPMS.2018.2864923.

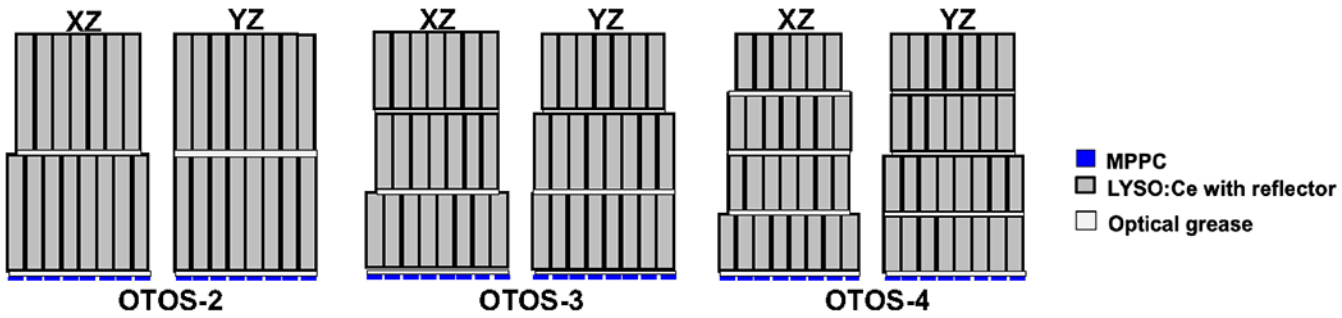

Figure 1.

Schematic drawing of the detector configurations based on staggered crystal layers with one-to-one coupling between the first layer and the photodetector array. Each layer is offset from its neighbors with half pixel pitch in one dimension. The same crystal configurations are explored also with light sharing between the first layer and the photodetector, according to the readout schemes illustrated in Figure 2.

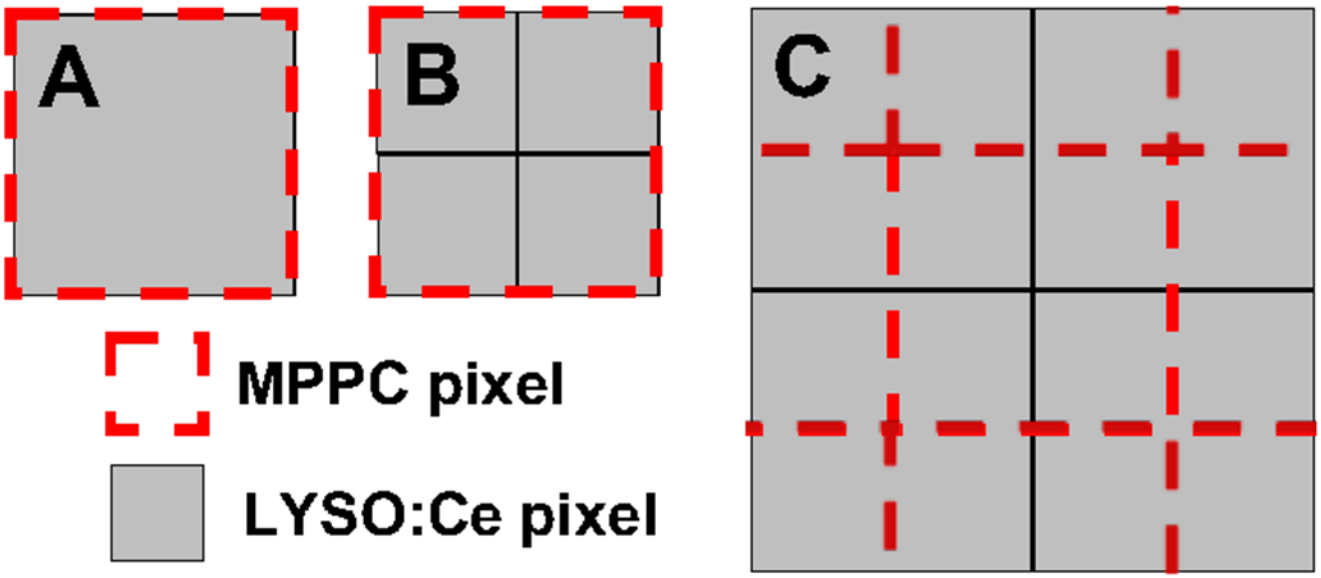

Figure 2.

Schematic illustration of the arrangements of MPPC pixels with respect to the crystal pixels in the bottom layer of the crystal stack. Three configurations were simulated: A) MPPC pixels and crystal pixels aligned and of same size. B) Crystal pixels smaller than MPPC pixels with 4 crystal pixels per MPPC pixel. C) MPPC pixels and crystal pixels of same size but offset by half pixel pitch in both X and Y directions. Configurations B and C correspond to light sharing readout schemes and a 1 mm light guide is used between the first crystal layer and the MPPC. Configuration A corresponds to one-to-one coupling and in this case no light guide is used.

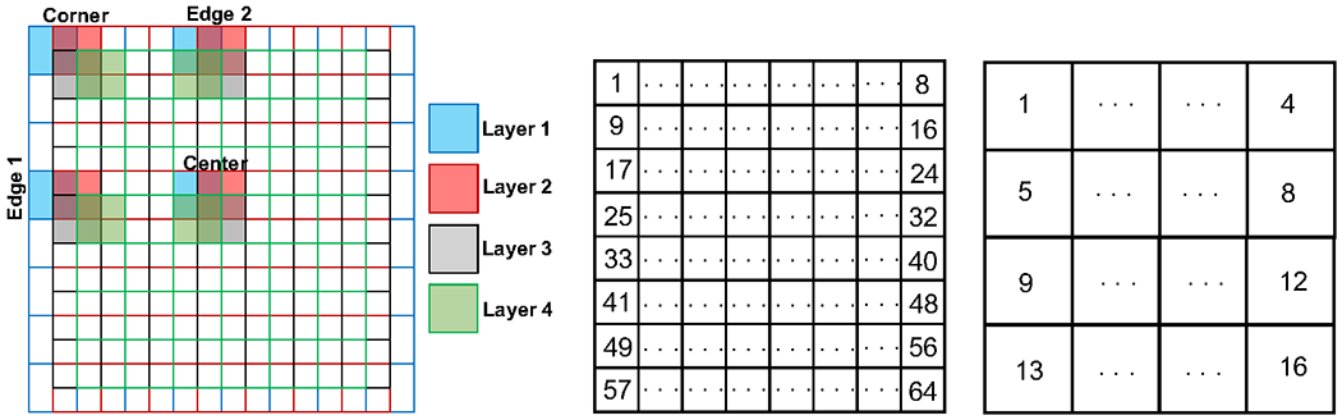

Figure 3.

Left: Naming convention and pixel locations where gamma events were simulated. Layer 1 is closest to the photodetector plane. Middle: MPPC pixel indices for the 8x8 MPPC arrays with 2.2- and 3.2-mm pitch. Right: MPPC pixel indices for the 4x4 MPPC array with 4.2 mm pitch.

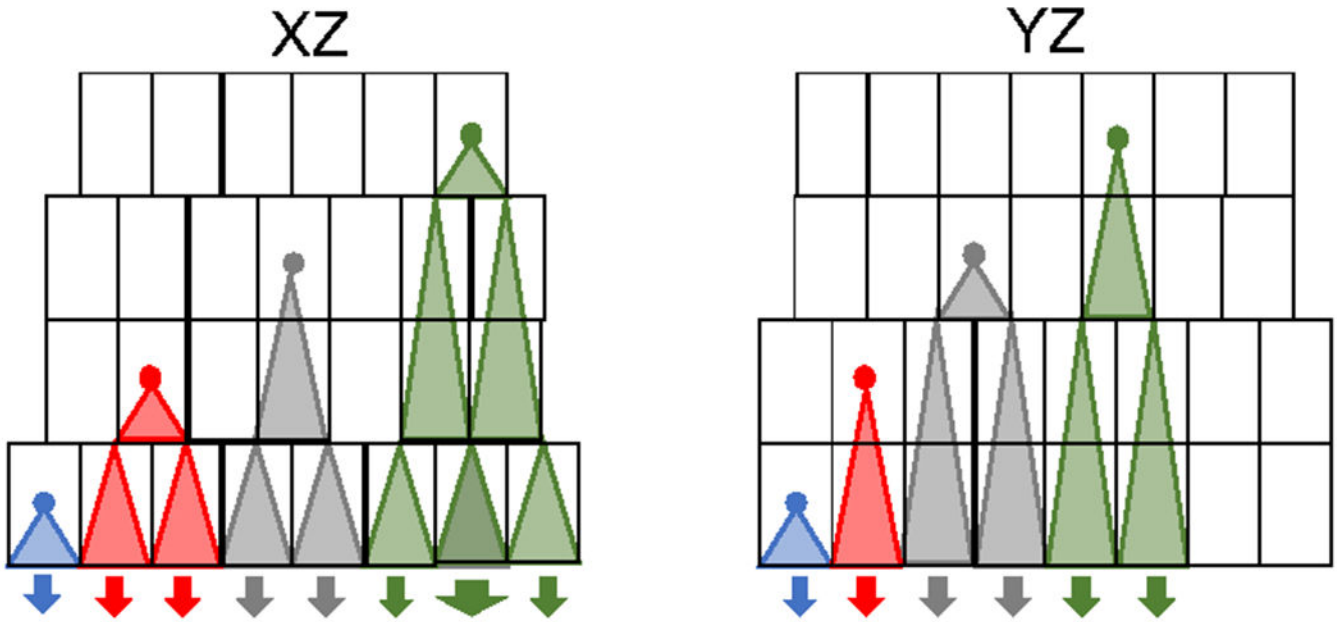

Figure 4.
Illustration of the light spread from each of the layers in two dimensions for the OTOS-4 configuration.

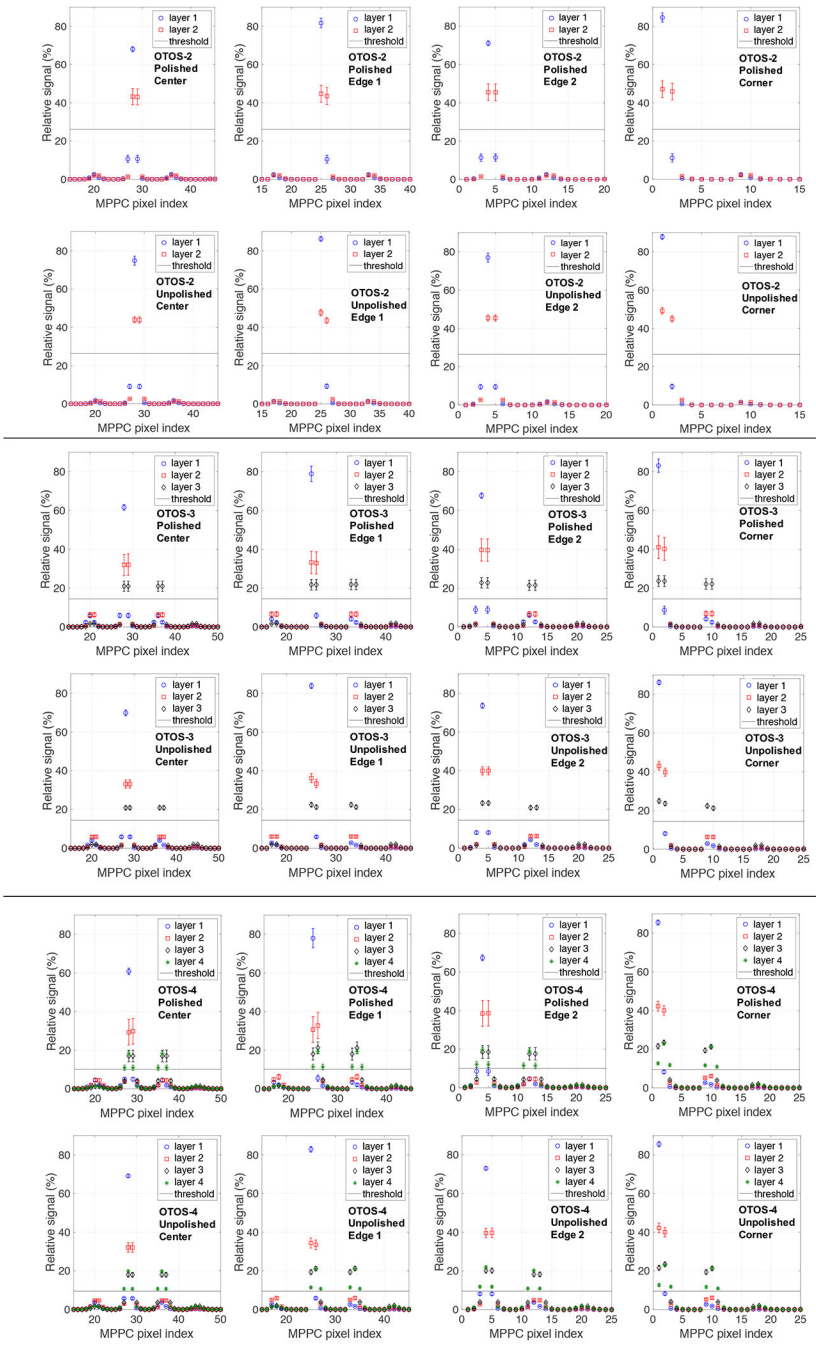

Layer	# Signals > threshold
1	1
2	2

Layer	# Signals > threshold
1	1
2	2
3	4

Layer	# Signals > threshold
1	1
2	2
3	4
4	6

Figure 5.

Average light distributions per detector layer for the OTOS-2, 3 and 4 designs calculated from all events within a given pixel in a given layer. Shown are distributions for 4 representative locations, as described in Figure 3. Values are the percentage of the sum signal, and the error bars correspond to one standard deviation around the mean values. For each configuration results are shown for both polished and unpolished crystal pixels. Top: OTOS-2, Middle: OTOS-3, Bottom: OTOS-4. The correspondence between source location and MPPC pixel index is illustrated in Figure 3. Note that, for better visualization, the signal

amplitudes of all 64 MPPC channels are not shown in each plot. Signals outside the shown X-range were negligible. The threshold used for DOI positioning is also indicated in each subplot.

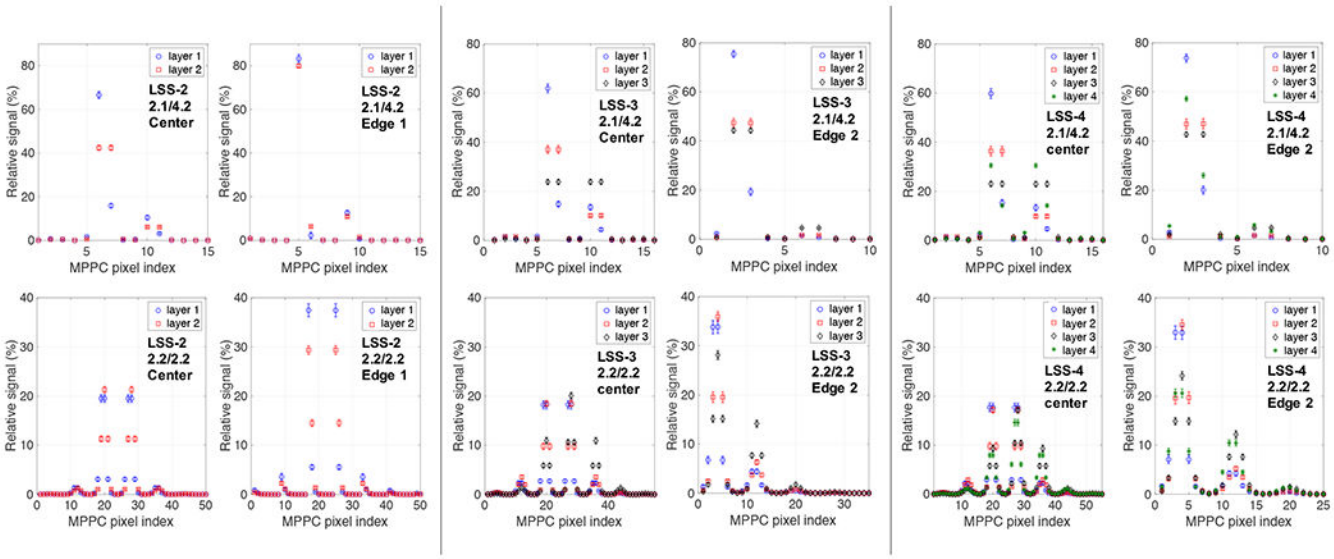

Figure 6.

Average light distributions for the LSS configurations. Shown are results for a central and an edge pixel for the LSS 2.1/4.2 pitch and the LSS 2.2/2.2 pitch light sharing schemes. Left: LSS-2, middle: LSS-3, right: LSS-4.

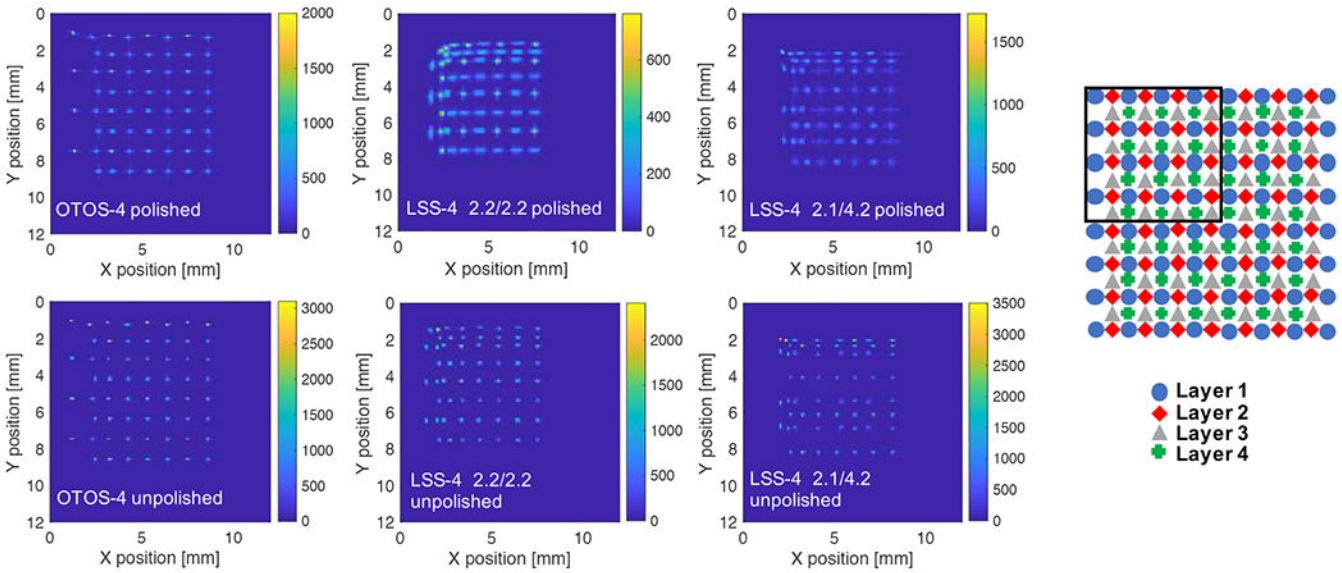

Figure 7.

Left: Flood maps for the 4-layer detector configurations. Right: Schematic picture showing the corresponding pixel for each of the event clusters in the OTOS-4 flood maps. The maps contain events from all simulated interaction depths and were generated using the center of gravity method as outlined in Section 2.4. Note that due to symmetry, events were only simulated in one quarter of the detector, indicated by the square in the schematic. Accordingly, the flood maps also only show events in one quarter of the detector.

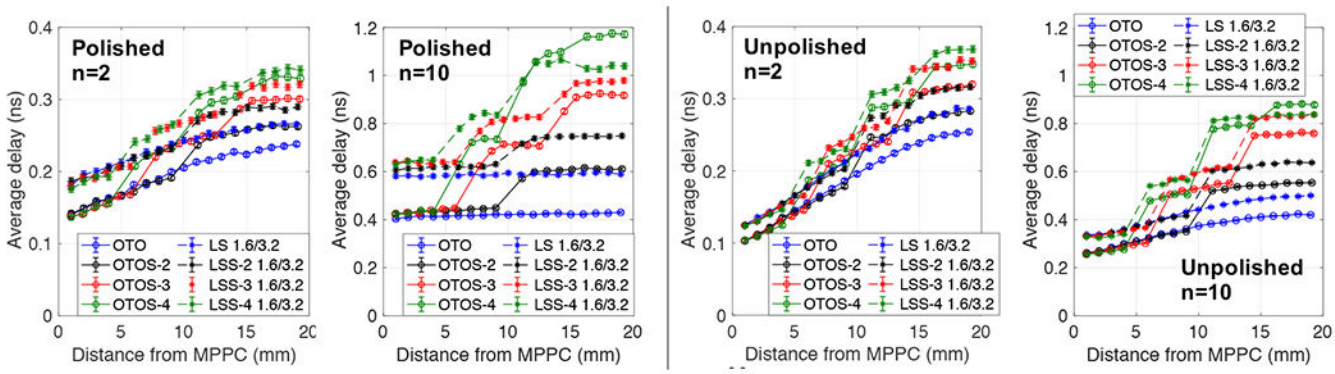

Figure 8.

Average delay in detection of the *n*'th optical photon in the MPPC pixel that is first to exceed the threshold defined by *n*. Here the proposed OTOS configuration is compared to LSS 1.6/3.2, being the intermediate version of the light sharing schemes simulated in this paper. The delay is shown as a function of depth and was determined by Gaussian fit to the distribution of events at the given depth. Here only the performance in the center of the array is shown. Error bars correspond to the 95% confidence interval in the fit parameter. Two different thresholds are shown, corresponding to 2 and 10 optical photons, and results are shown for polished (Left) and unpolished crystal pixels (Right).

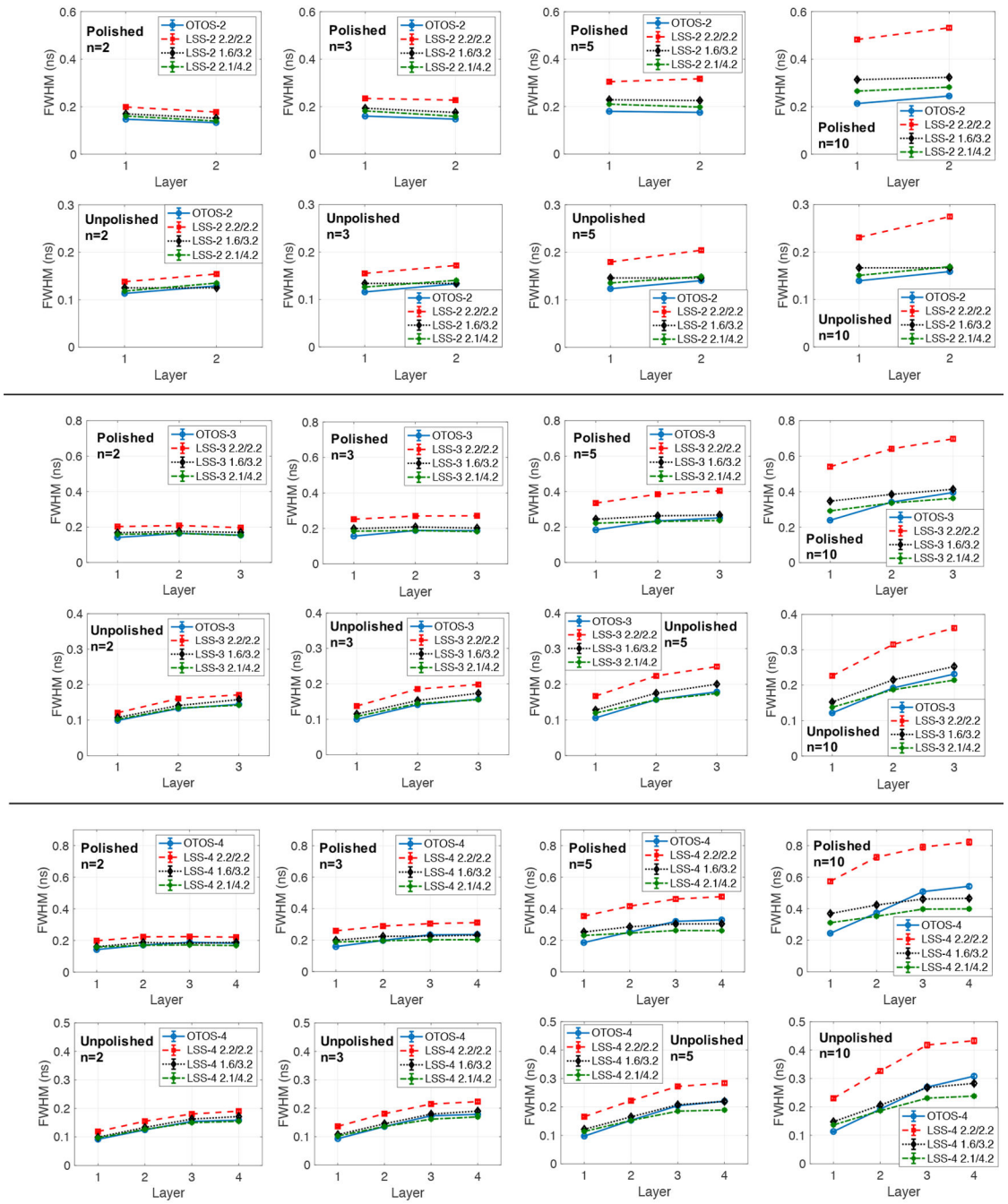

Figure 9.

Comparison of time jitter across events in a given crystal layer. Shown is data from events within a central pixel in the 2-layer (top), 3-layer (middle) and 4-layer (bottom) designs with different readout schemes. The FWHM values were determined by Gaussian fit to the distribution of events at the given layer. Error bars correspond to the 95% confidence interval in the fit parameter. Four different thresholds are shown corresponding to 2, 3, 5 and 10 optical photons, and results are shown for polished and unpolished crystal pixels.

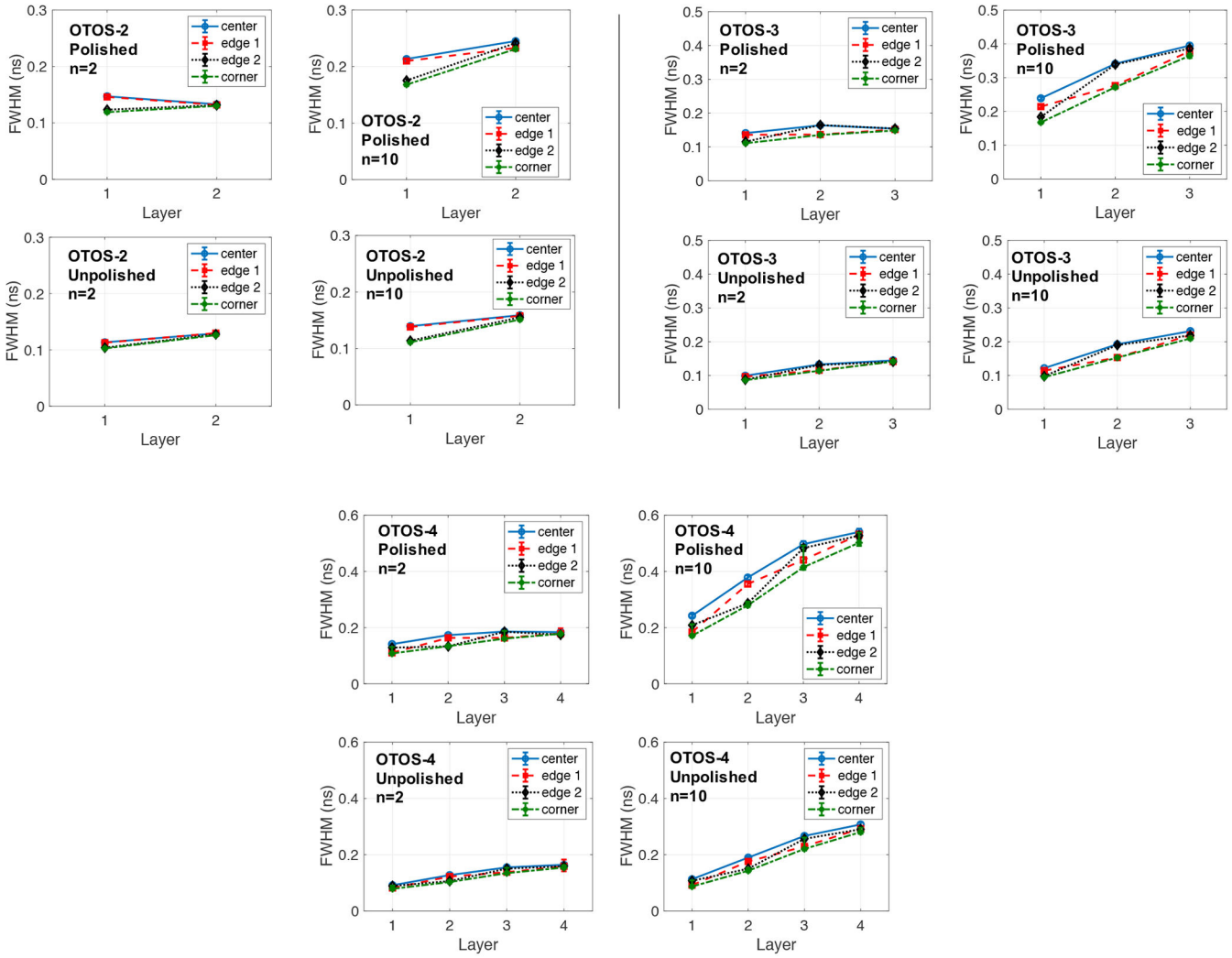

Figure 10.

Comparison of time jitter across events in a given layer for the proposed OTOS-2,3 and 4 designs. Timing performance is compared across central, edge and corner pixels, as defined in Figure 3. The FWHM values were determined by Gaussian fit to the distribution of events at the given layer. Error bars correspond to the 95% confidence interval in the fit parameter. Results for two different thresholds are shown corresponding to 2 and 10 optical photons, and results are shown for polished and unpolished crystal pixels.

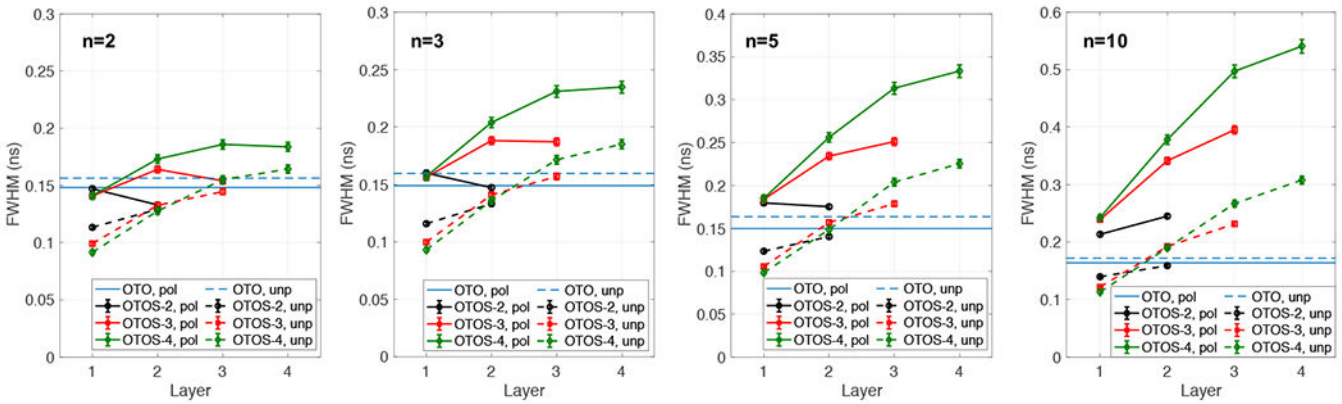

Figure 11.

Comparison of timing performance of the OTOS-2,3 and 4 designs as a function of number of layers, surface quality and threshold *n*. Note that the 4 graphs have different y-axes in order to better highlight the features in the presented data.

Table 1.

Summary and naming convention for the simulated detector configurations.

Category	Abbreviation	#of Crystal Layers	Pixel side surface properties	Pixel pitch (mm) Crystal/MPPC	Crystal-MPPC coupling (See Figure 2)
One-**T**o-**O**ne readout of single array	OTO	1	Polished, Unpolished	2.2/2.2	A
One-**T**o-**O**ne readout of **S**taggered arrays	OTOS-2,3,4	2,3,4	Polished, Unpolished	2.2/2.2	A
Light **S**haring readout of single array	LS	1	Polished, Unpolished	2.2/2.2, 1.6/3.2, 2.1/4.2	B or C
Light **S**haring readout of **S**taggered arrays	LSS-2,3,4	2,3,4	Polished, Unpolished	2.2/2.2, 1.6/3.2,2.1/4.2	B (1.6/3.2, and 2.1/4.2) or C (2.2/2.2)

Table 2.

DOI positioning accuracy for the OTOS designs, using the algorithm outlined in Section 2.4.

Geometry	Polished		Unpolished	
	Threshold (%)	Positioning Accuracy (%)	Threshold (%)	Positioning Accuracy (%)
OTOS-2	26.1	Center: 100 / 99.9 Edge 1: 100 / 99.9 Edge 2: 100 / 100 Corner: 100 / 100	26.4	Center: 100 / 100 Edge 1: 100 / 100 Edge 2: 100 /100 Corner: 100 / 100
OTOS-3	14.5	Center: 100 / 98.7 / 96.2 Edge 1: 100 / 99.4 / 98.0 Edge 2: 98.1 / 100 / 99.0 Corner: 97.7 / 100 / 99.35	14.4	Center: 100 / 100 / 100 Edge 1: 100 / 100 / 100 Edge 2: 100 / 100 / 100 Corner: 100 / 100 / 100
OTOS-4	10.1	Center: 100 / 100 / 95.03 / 52.8 Edge1: 99.6 / 99.0 / 100 / 68.7 Edge2: 74.4 / 100 / 97.9 / 81.4 Corner: 83.1 / 98.3 / 100 / 81.4	9.5	Center: 100 / 100 / 100 / 97.6 Edge1: 100 / 100 / 100 / 99.1 Edge 2: 91.2 / 100 / 100 / 99.9 Corner: 93.0 / 100 / 100 / 100

Table 3.

Average LCE (%), as defined in Section 2.4., in the center of the array for the OTO/OTOS detector configurations. Uncertainties correspond to one standard deviation in the variation between individual events in the center of the array, throughout the detector thickness.

	Polished	**Unpolished**
OTO	34.0 ± 0.7	69.8 ± 2.4
OTOS-2	32.9 ± 0.7	66.4 ± 3.8
OTOS-3	31.8 ± 0.9	63.1 ± 5.1
OTOS-4	30.8 ± 1.2	60.1 ± 6.2

Table 4.

Average LCE (%) in the center of the array for the LS/LSS detector configurations. Uncertainties are determined as in Table 3.

	Pitch 1.6/3.2		Pitch 2.1/4.2		Pitch 2.2/2.2	
	Polished	**Unpolished**	**Polished**	**Unpolished**	**Polished**	**Unpolished**
LS	34.0 ± 0.7	65.3 ± 3.8	34.4 ± 0.7	70.0 ± 2.7	32.0 ± 0.7	64.9 ± 2.4
LSS-2	32.7 ± 0.9	60.7 ± 5.6	33.6 ± 0.7	66.4 ± 4.2	31.1 ± 0.7	61.8 ± 3.8
LSS-3	31.3 ± 1.1	56.4 ± 7.1	32.2 ± 0.9	62.2 ± 5.6	30.0 ± 0.9	58.9 ± 4.9
LSS-4	30.1 ± 1.4	53.1 ± 8.6	31.3 ± 1.2	59.9 ± 6.8	29.0 ± 1.1	56.1 ± 5.9

Table 5.

Variation of LCE across the detector cross section for the OTOS configurations, with polished and unpolished pixels. Source locations are defined as illustrated in Figure 3. All values are shown in %.

	Polished				Unpolished			
	Center	**Edge 1**	**Edge 2**	**Corner**	**Center**	**Edge 1**	**Edge 2**	**Corner**
OTOS-2	32.9 ± 0.7	33.3 ± 1.3	32.9 ± 0.9	33.3 ± 1.3	66.4 ± 3.8	69.3 ± 5.8	66.7 ± 4.0	69.8 ± 6.0
OTOS-3	31.8 ± 0.9	31.8 ± 1.8	32.0 ± 1.3	32.2 ± 2.0	63.1 ± 5.1	65.3 ± 7.8	65.3 ± 5.8	67.6 ± 8.0
OTOS-4	30.8 ± 1.2	31.2 ± 2.1	30.9 ± 1.9	31.2 ± 2.6	60.1 ± 6.2	63.5 ± 8.7	62.3 ± 7.9	65.5 ± 9.7

Table 6

Average timing resolution values (ns) for the OTO(S) designs, oriented with the top crystal layer facing the gamma source.

	***n*=2**		***n*=3**		***n*=5**		***n*=10**	
Configuration	**Polished**	**Unpolished**	**Polished**	**Unpolished**	**Polished**	**Unpolished**	**Polished**	**Unpolished**
OTO	0.148	0.156	0.149	0.160	0.150	0.164	0.164	0.172
OTOS-2	0.137	0.124	0.150	0.128	0.176	0.135	0.235	0.153
OTOS-3	0.155	0.133	0.182	0.142	0.235	0.160	0.352	0.201
OTOS-4	0.178	0.146	0.219	0.161	0.296	0.191	0.464	0.253